Hydrogen in methanol catalysts by neutron imaging

Terreni, Jasmin; Billeter, Emanuel; Sambalova, Olga; Liu, Xiaochun; Trottmann, Matthias; Sterzi, Andrea; Geerlings, Hans; Trtik, Pavel; Kaestner, Anders; Borgschulte, Andreas

DOI
10.1039/d0cp03414b

Publication date
2020

Document Version
Accepted author manuscript

Published in
Physical Chemistry Chemical Physics

PCCP

ARTICLE TYPE

Cite this: DOI: 00.0000/xxxxxxxxxx

Hydrogen in Methanol Catalysts by Neutron Imaging

Jasmin Terreni,[*a,b] Emanuel Billeter,[a,b‡] Olga Sambalova,[a,b] Xiaochun Liu,[a,b] Matthias Trottmann,[a,b] Andrea Sterzi,[a,b] Hans Geerlings,[c] Pavel Trik,[d] Anders Kaestner,[d] and Andreas Borgschulte[a,b]

Received Date
Accepted Date

DOI: 00.0000/xxxxxxxxxx

Although of pivotal importance in heterogeneous hydrogenation reactions, the amount of hydrogen on catalysts during reaction is seldom known. We demonstrate the use of neutron imaging to follow and quantify hydrogen containing species in Cu/ZnO catalysts *operando* during methanol synthesis. Steady-state measurements reveal that the amount of hydrogen containing intermediates is related to the reaction yields to CO and methanol, as expected from simple considerations of the likely reaction mechanism. Time-resolved measurements indicate that these intermediates, despite indispensable within the course of reaction, slow down the overall reaction steps. Hydrogen-deuterium exchange experiments indicate that hydrogen reduction of Cu/ZnO nano-composites modifies the catalyst in way that at operating temperature hydrogen is dynamically absorbed in the ZnO-nanoparticles. This explains the extraordinary good catalysis of copper if supported on ZnO by its ability to act as a hydrogen reservoir supplying hydrogen to the surface covered by CO_2, intermediates, and products during catalysis.

1 Introduction

The production of methanol from syngas is an established chemical process utilized on an industrial scale using highly efficient Cu/ZnO nanocatalysts.[1] With the advent of a worldwide renewable energy scenario, the production of methanol from CO_2 and renewable hydrogen is receiving increasing attention.[2,3] This reaction is catalyzed by similar catalysts.[4] Although long known, the reaction mechanism, in particular intermediates and relevance of the complex and very specific nano-structure of the catalysts are debated.[5,6]. Recently, the careful structural analysis of such industrial Cu/ZnO catalysts triggered the hypothesis that zinc oxide has the ideal reducibility to catalyze methanol synthesis, which was found to be a consequence of the stability of the Cu/ZnO nano composite with the right bulk defects, and peculiar interface and surface structures.[5] The authors concluded that the functioning of the methanol catalyst "could be further evaluated if a method of quantitatively relating the reducibility to the catalytic properties could be found."[7] Traditionally, reducibility is experimentally assessed by the method temperature programmed reduction (TPR), in which the amount of hydrogen consumed and its temperature dependence to reduce the previously oxidized catalyst is determined. This method depends on many experimental factors, which can strongly vary.[1] An elegant way using model systems was introduced by Karim et al.[8] The study emphasizes the strong link between reducibility of the support and hydrogen spillover. The challenge of all experimental methods is the determination of the exact amount and dynamics of hydrogen in/on the material during reaction.[9] As hydrogen has only one electron, its detection by analytical tools based on the interaction with electrons is challenging: core-level spectroscopies such as X-ray photoelectron spectroscopy[10] and X-ray absorption[11,12] cannot be used as a quantitative method for hydrogen, and hydrogen is nearly invisible for X-ray diffraction.[13,14] A reliable probe must thus make use of the interaction with the proton, which is possible by nuclear magnetic resonance[15,16] and neutron techniques. We demonstrate in this paper the use of neutron imaging to follow the number of hydrogen species *operando*. The interaction of neutrons with many types of materials is relatively weak,[17] and thus, for example, a neutron beam can easily penetrate thick aluminum walls of a chemical reactor. At the same time, neutrons have a large cross section with hydrogen, i.e., we can probe hydrogen in an operating chemical reactor.[18] Neutron imaging allows the quantification of the absolute amount of hydrogen containing compounds on a catalyst over the course of the reaction,[19] and by relating to the surface area, the number of occupied sites is estimated. A drawback of the method is that it cannot provide the information, which exact molecule is adsorbed. There

[a]*University of Zurich, Department of Chemistry, Winterthurerstrasse, 190, CH-8057 Zürich, Switzerland.*
[b]*Empa, Swiss Federal Laboratories for Materials Science and Technology, Laboratory for Advanced Analytical Technologies, Überlandstrasse 129, CH-8600 Dübendorf, Switzerland.*
[c]*Delft University of Technology, Department of Chemical Engineering, 2629 HZ Delft, The Netherlands*
[d]*Laboratory for Neutron Scattering and Imaging (LNS), Paul Scherrer Institut (PSI), CH-5232 Villigen PSI, Switzerland*

are various possibilities: chemisorbed hydrogen, OH-groups, intermediates, and the products water and methanol.[20,21] We shed light on this uncertainty by simultaneously measuring the product yield as a function of partial pressures, temperature and time by gas IR-analysis. The amount of mobile hydrogen on/in a catalyst is determined by neutron imaging of hydrogen deuterium exchange. In addition, we support the neutron experiments by hydrogen-deuterium exchange by laboratory experiments making use of the weight change upon hydrogen-deuterium exchange. The main outcome of the experiments is that hydrogen reduction of Cu/ZnO nano-composites modifies the catalyst in way that at operating temperature hydrogen is dynamically absorbed. This explains the extraordinary good catalysis of copper if supported by ZnO by its ability to act as a hydrogen reservoir supplying hydrogen to the surface covered by CO_2, intermediates, and products during catalysis.

2 Experimental

Samples. Commercial copper-based methanol synthesis catalysts $Cu/ZnO/Al_2O_3$ pellets from Alfa Aesar. Catalytic performance: max at ca. 225°C = 0.0145 mmol CH_3OH min^{-1} = 0.128 kg MeOH (kg cat)$^{-1}$ h^{-1}; space velocity = 60000 l h^{-1}.

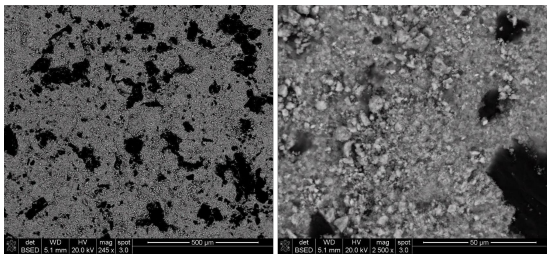

Fig. 1 Scanning electron microscopy images of the catalysts at two different magnifications. The blacks spots are identified as empty space.

X-ray diffraction (XRD) patterns were carried out on a PANalytical X'Pert-Pro powder X-ray diffractometer, using Cu Kα monochromatized radiation (1.541) between $2\theta = 10^{\circ}90^{\circ}$ (X-ray gun setting at 40 kV and 40 mA). The XRD powder pattern

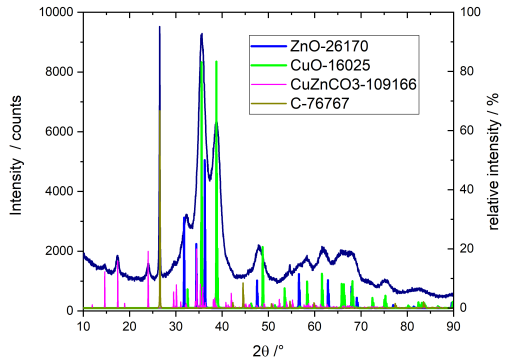

Fig. 2 X-ray diffraction pattern of the Cu/ZnO/Alumina catalyst.

of the studied catalyst (Fig. 2) shows broad diffraction lines corresponding to monoclinic CuO (ICDD-PDF 16025) and ZnO (ICDD-PDF 26170). Crystalline Rosasite (CuZn)2CO3; ICDD-PDF 109166 as well as graphite (ICDD-PDF 76767) are identified and explain the low infrared reflectivity of the samples (see DRIFTS discussion below). Interestingly, we do not observe peaks related to alumina, which is thus X-ray amorphous. The observations are in good agreement to the one found for similar Cu/ZnO/alumina catalysts as studied in Refs.[22,23]

Surface characterization. The total surface area was determined by BET (micrometrics ASAP 2000) to be 105 m^2/g. The copper surface area was determined by hydrogen reduction/N_2O oxidation cycles.[24] The freshly reduced catalyst is exposed to N_2O. Simultaneously, the weight change is recorded and normalized by the atomic weight of oxygen and total weight of the sample. Assuming that only the two uppermost atomic layers of the Cu nano-particles are oxidized, i.e. $[Cu]/[O] = 1$,[22] one can relate the weight change to the number of Cu surface atoms giving a Cu surface area of 18 m^2/g, in good agreement with literature.[22] Experimental conditions: Rubotherm magnetic suspension balance, Rubotherm Bochum, reducing in H_2 at 300°C, cooling down to 100°C, He for 1 h, N_2O for 30 min, He for 1 h.

Neutron Imaging. High-resolution neutron imaging was performed at the cold neutron beamline ICON[25] at the Swiss Neutron Spallation Source (SINQ), PSI (Switzerland).[26] The SINQ neutron source operated at 1.33 mA delivering polychromatic neutrons in the thermal to cold energy range. The beam defining aperture at ICON beamline was 20 mm in diameter and the imaging detector was placed at the measuring position No. 2. The collimation ratio (L/D) was equal to approximately 350. After traversing the sample position, the neutron beam was captured by 20 μm thick Gadolinium oxysulfide scintillator screen. The scintillation light has been collected using fibre optics taper (FOT)[27] in contact to the scintillator screen by its small end. The light emitted from the large end of the FOT has been detected using standard camera box (MIDI box) using a 100 mm Zeiss Makro-Planar objective and a 2048 x 2048 charged couple device (Andor Technology). The resulting pixel size of the acquired images was equal to 6.2 micrometres and the spatial resolution was assessed visually by imaging Siemens star test pattern[28] was equal to approximately 20 micrometres. The sample (Cu/ZnO pellet) was placed in a heated reactor cell made of aluminum, near to the scintillator plate at around 20 mm distance, and aligned to have the pellet's cylindrical axis parallel to the neutron beam. The exposure times of the individual neutron images was equal to 20 s. For measurements under static conditions, 10 images were averaged for better statistics. The image analysis was performed using the software ImageJ using built-in functions and a plug-in for image normalization developed by the Neutron Imaging and Applied Materials Group at PSI.

The total neutron attenuation coefficient σ_{tot} was calculated using the sum of total neutron scattering cross section (coherent plus incoherent) and of the neutron absorption coefficient.[17] With the setup used for neutron imaging (thermal neutrons with broad energy range), the attenuation coefficients do not depend significantly on the chemical nature of the species.[29]

Gas supply and Analysis. The gas (reactants) flows were controlled by thermal mass flow meters from Bronkhorst connected to a Labview interface. Typical flow rates were 25 ml min^{-1} CO_2, and 100 ml min^{-1} H_2 (and deuterium, respectively). The product gases were led through an FTIR-gas cell installed at a Bruker Alpha spectrometer acquiring spectra at a resolution of 0.8 cm^{-1}. Gravimetric analysis was performed in a Rubotherm Magnetic Suspension balance (Bochum, Germany) attached to the same gas supply system.[30]

Diffusive reflectance infrared Fourier Transform Spectra (DRIFTS) were collected using a Vertex 70 infrared spectrometer (Bruker Optics) equipped with a DRIFT unit (Praying Mantis, Harrick) and liquid nitrogen cooled MCT detector. The commercial Harrick cell (HVC-DRP-3) was attached to the same gas manifold system used for neutron imaging (see above). DRIFTS

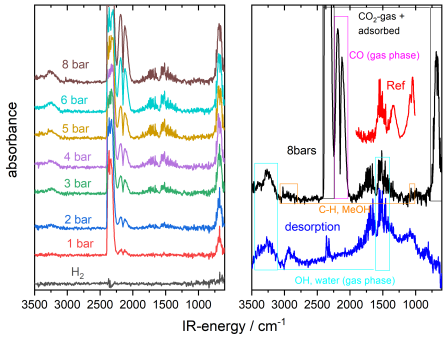

Fig. 3 DRIFTS experiments on Cu/ZnO/Alumina catalyst hydrogen /CO_2 mixture (1:3) up to 8 bar. The panel highlights the 8 bar spectrum, and the one after stopping CO_2 flux showing remaining adsorbates. The reference spectrum (at 1 bar H_2/CO_2) is taken from Ref. [31].

was already be used to identify the main reactants, intermediates, and products adsorbed on the surface as well as in the gas phase during CO_2 reduction on Cu/ZnO-alumina.[32,33] However, due to large carbon content and various nano-crystalline (see Fig. 2), the infrared reflectivity of the sample is extremely low, and the observed changes originate mainly from reactants and products in the gas phase. Furthermore, bulk phases such as rosasite ($CuZn(OH)_2(CO_3)$) may influence the DRIFTS signal, if they are modified during reduction/reaction.

3 Results and discussion

Figure 4 explains the idea of neutron imaging for catalysis along experimental neutron images of an industrial methanol catalyst consisting of a pellet with 5.4 mm diameter and 3.6 mm height (see photo). The pellet is inserted into a heated aluminum reactor. The neutron beam is attenuated while travelling through the sample/sample holder. With 1.7 barn[17,34], the total neutron attenuation coefficient (see section *Experimental*) for aluminum is low, but not negligible. Thus, the bore of the reactor is visible on a neutron transmission image as a brighter area (Fig. 4). The total neutron attenuation coefficient for Cu (11.81 barn) and Zn (5.24

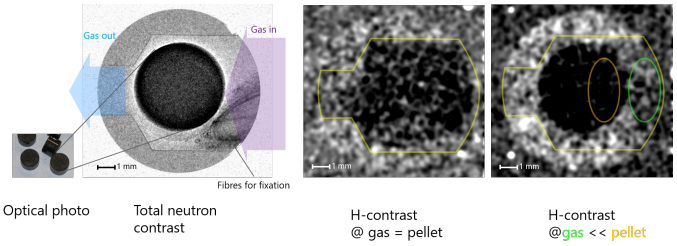

Fig. 4 Neutron transmission image of a Cu/ZnO catalyst pellet (optical photo on the left) placed in an aluminum reactor (left large picture). Middle and right pictures show the neutron contrast image at different conditions, one with hardly any excess hydrogen adsorption in the catalyst, (middle), and one with marked adsorption in the catalyst exceeding that of the gas phase (right). The contrast is maximized for each image for better visibility. The yellow line is a guide to the eyes to indicate the reactor bore.

barn) is higher[17], and thus the catalyst pellet placed inside the bore appears as black disk. This image serves as reference image (= reference signal I_0). During reaction, the gas content as well as adsorbed species changes. Possible elements are hydrogen, oxygen and carbon with absorption cross sections of 82.35 barn, 4.23 barn, and 5.55 barn, respectively.[17] Effectively any changes of the neutron attenuation can thus be related to a changes of the number of hydrogen atoms. The changes of the hydrogen content x_H are recorded as a deviation from the reference image $I_{t=0}/I_0$. This deviation is quantified by applying the Lambert–Beer law:

$$\ln\left(\frac{I_0}{I}\right) = x_H \cdot d \cdot \mu \qquad (1)$$

d is the thickness of the disk, μ is the molar cross section. This approach is possible because the neutrons transmit the sample in the direction of the pellet's cylinder axis. Figure 4 shows two typical examples: one, in which hydrogen adsorption in the sample is negligible also at high hydrogen gas pressure, and one with high hydrogen load in the sample.

In the first case, the sample is exposed to H_2 at higher pressure than used while taking the background image. Due to the increased number of hydrogen atoms in the gas phase, the whole bore appears as dark area. In this particular case, as there is no significant difference (contrast) to the pellet area, one can conclude that the amount of hydrogen in the gas phase is similar to the amount of hydrogen species on the catalyst. In second case, the catalyst is exposed simultaneously to CO_2 and H_2 (reaction conditions). Under these particular conditions, hydrogen containing species accumulate on the surface of the catalyst. These additional species lead to a comparably higher contrast at the pellet area compared to the gas phase. To separate the signals originating from gas and hydrogen in the catalyst, the gas signal is subtracted from the signal in the pellet, which contains both contributions, giving the "excess hydrogen" in the catalyst $x_H \propto \ln(I_{cat}/I_{gas})$. For experimental details, see section *Experimental*.

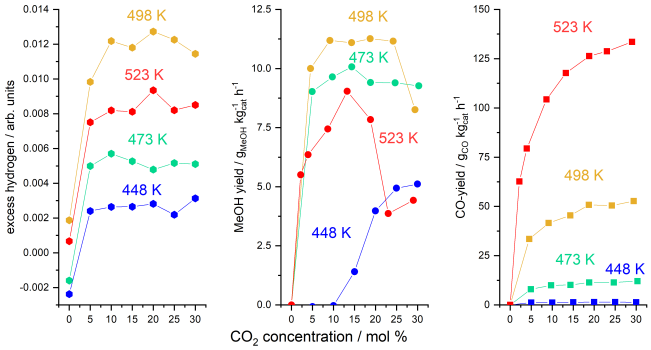

Fig. 5 Left graph: "excess hydrogen" $x_H \propto \ln I_{cat}/I_{gas}$ at 12 bar hydrogen as a function of the CO_2 concentration and temperature. Simultaneously, the MeOH-yield (middle graph) and CO-yield is determined (right graph). For the CO-yield, an Arrhenius analysis gives an activation energy of $E_A = 1.24$ eV ($\simeq$ 120 kJ/mol).

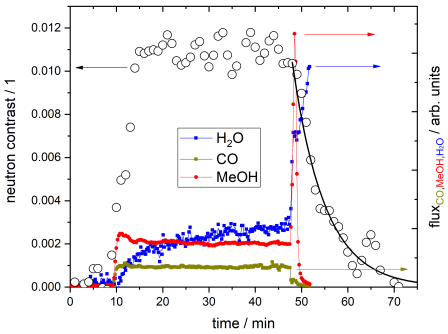

Fig. 6 Time resolved *operando* measurements: the neutron contrast as parameter of the amount of hydrogen containing adsorbates on the catalyst surface reaches steady-state rapidly after switching from H_2 to H_2/CO_2 mixtures as does the CO-yield. Contrarily, the MeOH yield has a maximum on the fresh sample, and the water signal slowly increases. Switching off CO_2 and reducing pressure to ambient conditions forces desorption of intermediates and products. The immediate decrease of the CO signal indicates that there is only little CO adsorbed, while the increase of MeOH and water proves that a substantial amount of MeOH-related intermediates and the products themselves are adsorbed as also visible by the rather slow decay of the neutron contrast (the line is a fit to an exponential function). Reaction conditions: $p = 12$ bar, T =473 K, H_2:CO_2 ratio 6:1.

3.1 Excess hydrogen during catalysis

The excess hydrogen plotted as a function of CO_2 concentration in Fig. 5 is the number of protons associated to the material. It may become negative as is the case for lower temperature at 0% CO_2, and indicates that the number of hydrogen atoms in the catalyst's volume is smaller than in the free gas space. These hydrogen atoms may be hydrogen attached to surface, including -OH species and -H on ZnO[35,36] as well as hydrogen chemisorbed on Cu,[20,37] which then transform into reaction intermediates and products, such as formate, acetal, and methoxy species[21,32,38] and water, methanol,[38] respectively. Neutron imaging as utilized here (white neutrons in the thermal energy range) cannot distinguish between differently bound hydrogens[39]. However, the larger amount excess hydrogen at finite CO_2 concentration is a consequence of the circumstance that the number of hydrogen atoms per adsorbate after reaction is higher than the ones formed in pure hydrogen. In the latter case, we expect only chemisorbed hydrogen (H^*) and hydroxide (OH^*), while during reaction hydrogen rich compounds are formed, e.g., $HCOOH^*$, H_2CO^*, H_3CO^*, H_3COH^* + H_2O^* (see discussion mechanism below). This hypothesis is further corroborated by the concentration dependence: the plateau-like behavior indicates that the reaction species are formed nearly independent of the actual gas concentration and reaction yield (compare simultaneously measured CO- and methanol-yield in Fig. 5, particularly at 448 K). That means that the surface coverage consists mainly of inactive, possibly even inhibiting adsorbates. Further evidence for this is given by time dependence of the process.

Time dependent measurements (Fig. 6) show that the complete removal, i.e., the desorption of intermediates and products from the surface takes up to one hour after switching from high pressure reaction conditions to pure hydrogen at 1 bar, while the coverage is completed within a few minutes after switching to reaction conditions. Main desorption product is water. Interestingly, also the methanol concentration peaks with pressure release, in contrast to CO, which just stops. Micro-kinetic models[38] emphasize the stability of some intermediates (such as OH forming eventually water, see below) on the surface of the catalyst blocking adsorption sites needed for catalysis. This explains the initially higher production yield as well as the absence of a concentration dependence of the coverage: a few percent CO_2 is sufficient to produce these adsorbates covering most of the surface of the catalyst.

Further insights on the chemistry taking place during catalysis may be concluded by comparison of the results with the ones supported by spectroscopic methods such as inelastic neutron scattering (INS)[40–42] and diffusive reflectance infrared Fourier transform spectroscopy (DRIFTS).[32,33] DRIFTS is a true *operando* spectroscopy, i.e., it is compatible with the particular sample form (usually powder) and sample environment (gas, liquid) at elevated temperatures and pressures.[43] However, the signals of the adsorbed as well as gaseous molecules depend on the IR-reflectivity of the catalyst.[44–46] Concretely, DRIFTS on 'black' (no-IR reflectivity) catalysts is very challenging.[47] We performed DRIFTS measurements (see section *Experimental*), but did not obtain meaningful information on surface adsorbates due to the extremely low infrared reflectivity of the sample.

From literature experiments and DFT-modelling[38] the following reaction mechanism were proposed (for illustration, see Fig. 9): CO-production proceeds via the reversed water gas shift (RWGS) reaction via a dissociative mechanism:[37,48,49]

$$CO_2 + H_2 + 3* \rightarrow CO + O^* + 2H^* \rightarrow CO + OH^* + H^* + * \rightarrow CO + H_2O + 3* \quad (2)$$

or via the associative mechanism:[50]

$$CO_2 + H_2 + 2* \rightarrow HCOO^* + H^* \rightarrow CO + OH^* + H^*$$

$$\rightarrow CO + H_2O + 2* \quad (3)$$

The dissociative mechanism is often called "redox" mechanism stems due the fact that there is an electron transfer involved from CO_2 to the adsorption site $*$ to form chemisorbed oxygen O^*. On Cu, this corresponds to the oxidation of Cu^0 to Cu^I. The role of hydrogen would then be to reduce the oxidized Cu back to Cu^0.[48] In principle, the first reaction step of the associative mechanism may proceed via Langmuir-Hinshelwood or via an Eley-Rideal pathway, possibly even concurrently as has been suggested for the RWGS on nickel.[49] However, for copper, there is strong experimental evidence that formate formation proceeds via the Eley-Rideal pathway, in which only hydrogen is chemisorbed at the surface, and CO_2 reacts from the gas phase or physisorbed state.[50]

A crucial difference between the processes 2 and 3 is the additional hydrogen containing intermediate (formate) that is formed during the associative pathway. In both reactions, water is formed and its reaction from OH* and H* is slow[38] and thus reduces the overall reaction yield. It is evident that the CO reaction yield depends on the partial pressure of CO_2 and hydrogen and on temperature to overcome the activation barrier,[37] as observed (Fig. 5). The measured yields and the from an Arrhenius analysis derived activation energy of approximately 1.24 eV (120 kJ/mol) are in good agreement with earlier studies (E_A = 1.6 eV (150 kJ/mol)[51]). In contrast, for the reduction of CO_2 to methanol at least six hydrogen containing species (HCOO*, HCOOH*, CH_3O_2*, CH_2O*, OH*, and CH_3O*) are formed on the surface of the catalyst according to the most probable pathway[38]:

$$CO_2 + 3H_2 \quad (4)$$

$$\rightarrow HCOO^* + 5/2\,((1-n)H_2 + 2nH^*) \quad (5)$$

$$\rightarrow HCOOH^* + 4/2\,((1-n)H_2 + 2nH^*) \quad (6)$$

$$\rightarrow H_2COOH^* + 3/2\,((1-n)H_2 + 2nH^*) \quad (7)$$

$$\rightarrow H_2CO^* + OH^* + 2/2\,((1-n)H_2 + 2nH^*) \quad (8)$$

$$\rightarrow H_2CO^* + HOH + 1/2\,((1-n)H_2 + 2nH^*) \quad (9)$$

$$\rightarrow H_3CO^* + H^* + H_2O \quad (10)$$

$$\rightarrow H_3COH + H_2O \quad (11)$$

n is the relative amount of hydrogen chemisorbed on the surface to that left in the gas phase. Without the reservoir of intermediates, methanol cannot be formed, which is in very good agreement with our experiment: highest methanol yield is found at highest amount of excess hydrogen. The lack of substantially adsorbed CO suggests an explanation of the need for CO_2 for CO hydrogenation to methanol: Even if direct pathways[38] may be available, the surface is covered by stronger binding adsorbates such as CO_2 and water. The neutron experiments are thus in agreement of the hypothesis that production of CO from CO_2 takes place via the associative pathway, although the results are not decisive.

The first step of the methanol synthesis and the associative mechanism of the RWGS reaction share formate as a common intermediate. Both reactions share another reaction step: the hydrogenation of OH* to form H_2O* and its subsequent desorption (eq. 9), which has a high barrier.[38] However, formation of CO depends on the partial pressure of CO_2, which rapidly decreases if the CO_2 supply is stopped (Fig. 6). Vice versa, methanol formation continues and the yield is even increased due to enhanced reaction of the still present intermediates with adsorbed hydrogen. Simultaneously, the water formation is markedly increasing, which continues even after complete reaction towards methanol. This is in line with the hypothesis that adsorbates such as OH^* block the chemisorption of hydrogen for reaction with CO_2, methanol intermediates and with OH^* itself. This fact is formally taken into account by introducing the variable n in the formulas 4 to 11, indicating that the ratio of chemisorbed hydrogen to hydrogen in the gas phase (n) is unknown. Various studies showed that hydrogen adsorption/desorption on Cu is fast compared methanol synthesis rates.[15] Hydrogen coverages of up to 40% at 10 bar were calculated. It is obvious, though, that chemisorbed hydrogen competes with other adsorbates for the same surface sites. Askgaard et al. give detailed values based on a micro-kinetic model:[52] at 50 bar and 500 K, the coverage by hydrogen $\theta_{H^*} = 0.330$ is significantly larger than that all other adsorbates: $\theta_{HCOO^*} = 0.070 > \theta_{CH_3CO^*} = 0.042 > \theta_{OH^*} = 0.017 > \theta_{CO^*} = 0.016 > \theta_{CO_2^*} = 0.0028 > \theta_{H_2O^*} = 0.0017 >> \theta_{rest}$. However, below this temperature, HCOO* is the most abundant species, with $\theta_{HCOO^*} \simeq 1$ eventually blocking all free sites. Thus, the high calculated rates of hydrogen chemisorption on Cu are existent as long further reaction with this chemisorbed hydrogen and eventually desorption of the formed intermediates is guaranteed.[15] The neutron data (excess hydrogen in Fig. 5) confirm experimentally that the surface is quickly equilibrated with additional hydrogen containing intermediates including water, which will reduce the hydrogen chemisorption rate.

In principle, the method gives absolute numbers. The number of hydrogen atoms per volume at 4 bar partial hydrogen pressure corresponds to $N_H/V = 2 \cdot 6 \cdot 10^{26} \cdot 4/(24 \cdot 10^{-3})$ m^{-3} $\simeq 2 \cdot 10^{29}$ m^{-3}. The surface area was 105 m^{2}g^{-1} (see *Experimental*), the density is around 5 g cm^{-3}, and the total surface atom density around $1.46 \cdot 10^{19}$ atoms per m^2. This gives the number of surface atoms per volume $N_{surf}/V = 2 \cdot 10^{29}$ m^{-3}. If we now measure a hydrogen excess of 0.01, we can estimate that 1% of the surface are covered by new species. Approximately 1/6 of the surface consists of Cu atoms (see *Experimental*). The order of the coverage is in good agreement with the numbers discussed above.[52] This estimation can be further specified using reference samples and/or reference states of the sample to be performed in the future.

Recently, a crucial difference between methanol synthesis from CO and hydrogen and methanol from CO_2 was traced back to the fact that only in the latter reaction water is formed and adsorbed at the surface and thereby blocking reaction sites.[53] The results at hand, both neutron imaging (Fig. 6) as well as DRIFTS, showing water as the only identifiable adsorbate (Fig. 3), corroborate this finding. The active removal of the product water is thus expected to enhance the reaction yield. This idea, also called sorption enhanced catalysis, was recently experimentally demonstrated (Cu/ZnO catalyst in ionic liquids[54], and Cu/zeolite

catalyst[55]).

3.2 Hydrogen on/in Cu/ZnO

The concentration of H* under methanol synthesis conditions is pivotal but cannot be measured easily due to interference with other hydrogen containing species. We have therefore studied the behavior of the catalyst in the absence of CO_2. To further increase the accuracy of our experiments, we combined neutron imaging with hydrogen-deuterium exchange. The hydrogen flow to the sample, which has been equilibrated at a given temperature and pressure, is abruptly exchanged for deuterium at the same conditions and later back to hydrogen again. Deuterium has a considerably lower neutron attenuation coefficient ($\sigma_{tot}(D) = 7.64$ barn, compared to $\sigma_{tot}(H) = 82.35$ barn),[17] and thus the neutron contrast ($\ln I_D - \ln I_H$) is directly proportional to the amount of hydrogen, which can be dynamically exchanged. With this technique, we can follow the kinetic measurements on the time scale of seconds (Fig. 7).

An advantage of the neutron technique is the imaging possibility, giving insights on diffusion processes. In zeolite based catalysts, we could show by this technique that macroscopic diffusion controls the reaction rate in catalyst pellets,[19] a very well-known constraint in technical catalysts.[56] However, on the accessible time and length scale of the experiments applied here, no difference of the time evolution at the outer and inner parts of the catalyst pellets are observed (Fig. 7). This indicates that the time dependence of the process stems from microstructural modifications, and the macroscopic transport through the pellet is too fast to be captured by neutron imaging with experimental parameters used. This conclusion is further corroborated by scanning electron microscopy images depicting the highly porous structure of the technical catalyst with voids of several 100 micrometer size (Fig. 1). On the other hand, the temporally accessible changes take place on length scales, which are not resolved by neutron imaging (below a micrometer). To still yield some insights into the atomistic changes, we only studied the time- and temperature dependence of the averaged hydrogen content on/in the catalyst. With neutron imaging being a very expensive technique, we highlight here a complimentary possibility for probing the H/D exchange. As deuterium has double the mass of hydrogen, the exchange of hydrogen can be gravimetrically determined (for details of the apparatus, see Ref.[30]). However, the $Cu/ZnO/Al_2O_3$ catalyst is not stable in hydrogen, it loses weight even after long equilibration (2 hours, see Fig. 7), which is attributed to the loss of oxygen by reduction of the ZnO. If now the hydrogen gas in the reactor is rapidly exchanged by deuterium, a steep weight increase is observed indictative of exchange of hydrogen by deuterium in the the sample. Reversing the process, the same negative weight difference is obtained. We compare the H/D exchange experiments using a magnetic suspension balance with the results from neutron imaging in Fig. 7. The steep changes upon gas changes (from hydrogen to deuterium and vice versa) are observed by both techniques and demonstrate the fast reversible exchange of hydrogen in Cu/ZnO. The difference to the neutron measurements is that in addition to mass changes from

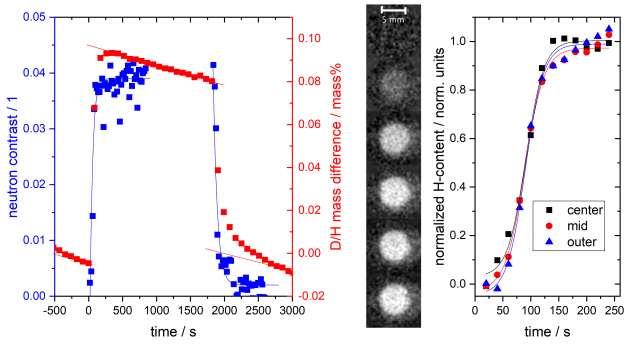

Fig. 7 Left graph: Change of neutron contrast and mass of $Cu/ZnO/Al_2O_3$ catalyst upon gas switch from hydrogen to deuterium and vice versa at 200°C. Right graph: time- and spatially resolved neutron contrast upon hydrogen deuterium exchange (at $t = 0$) derived from the neutron radiography image series ($t = 0, 25, 50, 75, 100, 250$ s) at three different location in the pellet (in the center, at half radius and at maximum radius).

H/D exchange mass changes occur from desorption of adsorbates and oxygen. This is visible by the linear decrease of the weight on top of the fast changes. Still, by substraction of this continuous change, the neutron contrast can be calibrated against the weight changes (compare also Fig. 8). In absolutely pure hydrogen, Cu/ZnO is unstable, and oxygen desorbs from the catalyst. This process starts around 450 K as usually determined by TPR.[57] The degree of reduction depends on the oxygen partial pressure. At temperatures below 800 K, only the surface of Cu/ZnO nanocatalysts is reduced,[20] if practical hydrogen (deuterium) purities are used: the threshold oxygen partial pressure of $p_{O_2} = 10^{-10}$ mbar corresponds to 13N hydrogen, which is technically unrealistic. We can thus assume that main part of the catalyst remains as ZnO, and only Cu, the direct vicinity of ZnO and its surface are reduced, as supported by numerous other studies[5,58] on Cu/ZnO (for enlightening discussion see Nakamura et al.[59]).

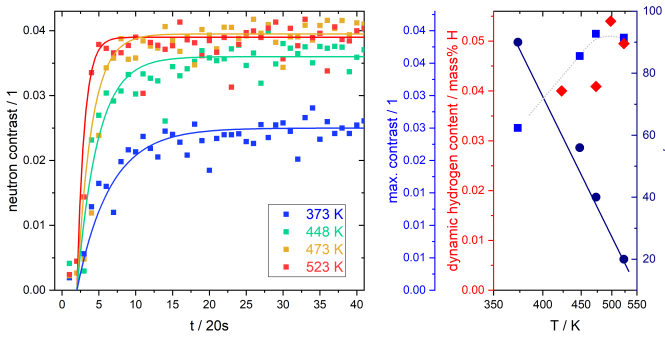

Fig. 8 Left panel shows the neutron contrast upon hydrogen-deuterium exchange in $Cu/ZnO/Al_2O_3$ catalyst at various temperatures yielding the kinetics of hydrogen mobility and total amount of hydrogen expressed by the amplitude (maximum contrast, blue squares) and time constant (dark blue spheres) derived from an exponential fit to the data, respectively. An Arrhenius analysis of the time constant (right panel) gives an activation energy of $E_A = 0.16$ eV. The maximum neutron contrast is compared to gravimetric H-D exchange measurements (red diamonds) calibrating the absolute amount of hydrogen in the sample.

An unexpected result is the increase of the maximum hydrogen content (maximum H/D exchange) with temperature. This is observed both by neutron imaging as well by gravimetric analysis (Figure 8). This additional weight change, which is practically subtracted from the sought signal, demonstrates that the hydrogen adsorption on the catalyst is coupled to the reduction of it. The observation of increasing hydrogen content with increasing temperature is counterintuitive: one expects a typical hydrogen ad/absorption curve[60] with the negative (exothermic) heat of adsorption and thus highest coverage is expected to occur at lowest temperature. Examples may be the well known dissociative adsorption of H_2 on Cu[61,62], while infrared studies unveiled the active sites for this dissociative adsorption of H_2 on pure ZnO as pairs of Zn and O surface atoms.[35] With $x \simeq 0$, the driving force for hydrogen uptake is the entropy gain, and then ΔH may be positive, too (Sieverts law):[63,64]

$$x_H \propto \sqrt{\frac{p}{p_0}} e^{-\frac{\Delta H_H}{k_B T} + \Delta S_H} \tag{12}$$

Such a behavior is observed in bulk absorption of hydrogen, i.e., ΔH_H and ΔS_H are the enthalpy and entropy of solution, respectively.

With this background information, it is possible to specify the kind of hydrogen on/in Cu/ZnO, being hydrogen **ad**sorbed on the surface, or **ab**sorbed in the bulk. Following table 1, hydrogen absorbed **in** ZnO is the most likely candidate matching the condition of a positive heat of absorption as well as a relatively high amount. The H-increase is evidenced by H/D exchange probed by neutron imaging as well as mass changes (Fig. 7); the observed mass loss at these temperatures indicates that also oxygen leaves the catalyst. The latter is evidence for some degree of surface reduction, as significant bulk reduction is expected at much higher temperatures only. In contrast to TPR-methods, neutron imaging together with gravimetric analysis allows to separate these two components of reducibility of a catalyst (hydrogen absorption and oxygen removal) usually only assessed by the one parameter hydrogen consumption.

Hydrogen absorption in ZnO is a well-known phenomenon; ZnO is a wide bandgap semiconductor with peculiar optoelectronic properties, which change upon hydrogen insertion.[65–69] An important question arises, whether this bulk hydrogen is relevant in catalysis. The kinetic measurements show an exponential behavior. We derived a time constant τ from an exponential fit to the kinetic curves (Fig. 8). With increasing temperature, the equilibrium is reached faster. An Arrhenius analysis gives an activation energy of $E_A = 0.16$ eV. Hydrogen dissociation on copper is activated with a barrier height of 1 eV.[70] First-principles electronic structure calculations predict a barrier height of $E_D \simeq 0.4$ eV for the *bulk diffusion* of hydrogen in ZnO,[68,69] i.e., the transport of hydrogen from dissociation sites on the surface via the bulk of the ZnO-nanoparticles to the reaction sites at the Cu-Zn interface is likely. One empirical indication is the total hydrogen uptake reaches its maximum, where the reaction yield towards methanol has its maximum. *Operando* neutron imaging shows a high amount of reaction intermediates and water, which block 'ordinary' hydrogen dissociation and chemisorption (Fig. 6) suggesting that hydrogen supply in methanol synthesis over Cu/ZnO catalysts is facilitated by spillover from ZnO to Cu, as suggested by Spencer et al.[15] The special 'promoter effect' of ZnO and other 'reducible' oxides such as In_2O_3 may thus be simply explained by the possibility of fast hydrogen transport through the bulk of the nano-support. This interpretation is in line with recent results on doped ZnO:[71] if the doping led to enhanced conductivity, catalytic activity is found to increase. As discussed above, hydrogen insertion increases conductivity.[65–69]

Various studies identified a peculiar nanostructure of Cu as well as ZnO and thus interface between Cu and ZnO formed during reduction and/or reaction as the reactive sites.[5,6,72] The findings of this study add an additional explanation of its relevance: it is straightforward to relate the overall catalytic activity to the surface area, as the number of potentially active sites scales with it. In addition, bulk diffusion can only be relevant to heterogeneous catalysis, if the diffusion path lengths are very short of the order of a few nanometer limiting the effect to nm-sized structures. This is in line with experiments of Nakamura et al.[73] and Studt et al.[74], who found that that already small amounts of Zn below the detection limit for bulk-ZnO are sufficient to promote Cu nanoparticles. Bulk hydrogen should thus be understood in the sense of sub-surface hydrogen. Further synergistic effects between Cu and Zn as suggested by the aforementioned papers are very likely, too, but cannot be studied by the methods utilized in this paper.

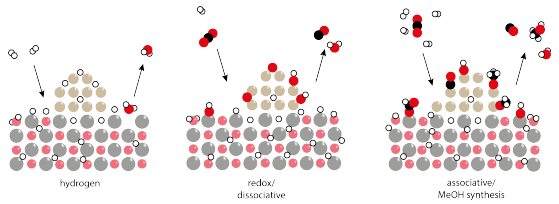

Fig. 9 Left panel: A sketch of a Cu/ZnO catalyst in pure hydrogen gas. Hydrogen is adsorbed on Cu and and on ZnO, as well as absorbed in ZnO and to a minor extent in Cu. There is consensus in literature that the Cu/Zn interface is metallic.[5] Catalyst reduction includes partial removal of oxygen by water formation as well. Middle and right panel: Cu/ZnO during catalysis. Main difference is that the surface is covered with reactants, intermediates, and products, and thus diffusion of hydrogen via the bulk becomes relevant. The positioning of the molecules is speculative. The middle panel sketches CO formation via the redox mechanism (2) and the right one displays CO and methanol formation via the associative pathway via $HCOO^*$ (3).

4 Conclusions

Using neutron imaging we are able to follow and quantify hydrogen containing species in Cu/ZnO during methanol synthesis. Steady-state measurements reveal that the amount of hydrogen containing intermediates is related to the reaction yields to CO and methanol, as expected from simple considerations of the likely reaction mechanism. Time-resolved measurements indicate that these intermediates, despite indispensable within the course of reaction, slow down the overall reaction steps. A disadvantage of neutron imaging is the lack of further chemical information other than the total amount of hydrogen. In com-

bination with the product gas analysis, DRIFTS, and literature, we show that water is one of the main adsorbates. The measurement of the total neutron scattering at operating conditions supported subsequently by INS on the same sample quenched to INS-compatible measurements[40,41,75] may be a future combination to overcome the experimental limitations of each individual method. In addition to hydrogen containing species during reaction, we probe the amount of hydrogen in the catalyst in pure hydrogen by H/D exchange. The analysis brings to the fore that a considerable amount of hydrogen is mainly located in the bulk of the ZnO nanoparticles, while traditionally "catalysts reduction" is associated with the removal of oxygen by water formation during hydrogen exposure at high temperature. As hydrogen can be rapidly exchanged in the catalyst, we propose that this absorbed hydrogen is relevant for catalysis via spillover to the active sites at the Cu/Zn interfaces, and not only a spectator. Although it was not intended, the difficulty in using DRIFTS on the same samples shows the robustness of the method, which has no experimental constraints like optical reflectivity limiting the use of DRIFTS and other optical *operando* methods.

Author contributions

J.T., E.B, O. S., A. S., A.B., A. K., and P. T. performed the neutron imaging experiments, X. L. and M. T. performed the characterisation of the catalysts, H. G. contributed to the analysis of the experiments, A.B. and P. T. defined and designed the concept of neutron imaging for catalysis, all authors contributed to writing of the study.

Conflicts of interest

There are no conflicts to declare.

Acknowledgements

This work was partly supported by the UZH-UFSP program LightChEC. Financial support from the Swiss National Science Foundation (grant nos. 144120 and 172662) is acknowledged.

Notes and references

1 I. Chorkendorff and J. Niemantsverdriet, *Concepts of Modern Catalysis and Kinetics*, Wiley-VCH Verlag GmbH & Co. KGaA, New York, 2007.

2 G. A. Olah, A. Goeppert and G. K. S. Prakash, *Beyond Oil and Gas: The Methanol Economy*, Wiley-VCH Verlag GmbH & Co. KGaA, Heidelberg, 2009.

3 B. Patterson and et al., *PNAS*, 2019, **116**, 12212–12219.

4 M. D. Porosoff, B. Yan and J. G. Chen, *Energy Environ. Sci.*, 2016, **9**, 62.

5 M. Behrens, *Science*, 2012, **759**, 893.

6 C. Tisseraud, C. Comminges, S. Pronier, Y. Pouilloux and A. Le Valant, *J. Catal.*, 2016, **343**, 106–114.

7 J. P. Greeley, *Science*, 2012, **336**, 810.

8 W. Karim, C. Spreafico, A. Kleibert, J. Gobrecht, J. VandeVondele, Y. Ekinci and J. A. van Bokhoven, *Nature*, 2017, **541**, 68–71.

9 T. Y. Wei, K. Lim, Y. S. Tsenga and S. L. I. Chan, *Renew. Sustain. Energy Rev.*, 2017, **79**, 1122–113383.

10 L. Nguyen, F. F. Tao, Y. Tang, J. Dou and X.-J. Bao, *Chemical Reviews*, 2019, **119**, 6822–6905.

11 M. A. Newton and A. J. Dent, in *In situ Characterization of Heterogeneous Catalysts*, ed. J. A. Rodriguez, J. C. Hanson and P. J. Chupas, John Wiley and Sons Inc, New Jersey, 2013, ch. Energy-Dispersive EXAFS: Principles and Application in Heterogeneous Catalysis, pp. 75–119.

12 J. A. van Bokhoven and C. Lamberti, in *XAFS Techniques for Catalysts, Nanomaterials, and Surfaces*, ed. Y. Iwasawa, K. Asakura and M. Tada, Springer International Publishing, Cham, 2017, ch. XAS Techniques to Determine Catalytically Active Sites in Zeolites: The Case of Cu-Zeolites, pp. 299–316.

13 H. Cheng, C. Lu, J. Liu, Y. Yan, X. Han, H. Jin, Y. Wang, Y. Liu and C. Wu, *Progress in Natural Science: Materials International*, 2017, **27**, 66 – 73.

14 F. Buchter, Z. Lodziana, A. Remhof, P. Mauron, O. Friedrichs, A. Borgschulte, A. Züttel, Y. Filinchuk and L. Palatinus, *Phys. Rev. B*, 2011, **83**, 064107.

15 M. S. Spencer, *Catal. Lett.*, 1998, **50**, 37.

16 L. Bouchard, S. Burt, M. S. Anwar, K. V. Kovtunov, I. V. Koptyug and A. Pines, *Science*, 2008, **319**, 442.

17 V. F. Sears, *Neutron News*, 1992, **3**, 26.

18 A. Borgschulte, R. Delmelle, R. B. Duarte, A. Heel, P. Boillat and E. Lehmann, *Phys. Chem. Chem. Phys.*, 2016, **18**, 17217.

19 J. Terreni, M. Trottmann, R. Delmelle, A. Heel, P. Trtik, E. H. Lehmann and A. Borgschulte, *J. Phys. Chem. C*, 2018, **122**, 23574–23581.

20 L. Martinez-Suarez, J. Frenzel, D. Marx, B. Meyer and L. Marti, *Phys. Rev. Lett.*, 2013, **110**, 086108.

21 S. Dang, H. Yang, P. Gao, H. Wang, X. Li, W. Wei and Y. Sun, *J. Catal.*, 2013, **330**, 61.

22 P. Kurr, I. Kasatkin, F. Girgsdies, A. Trunschke, R. Schlögl and T. Ressler, *Applied Catalysis A: General*, 2008, **348**, 153 – 164.

23 B. Liang, J. Ma, X. Su, C. Yang, H. Duan, H. Zhou, S. Deng, L. Li and Y. Huang, *Industrial & Engineering Chemistry Research*, 2019, **58**, 9030–9037.

24 M.-J. Luys, P. van Oeffelt, P. Pieters and R. Ter Veen, *Catalysis Today*, 1991, **10**, 283 – 292.

25 A. Kaestner and et al., *Nuclear Instruments and Methods in Physics Research Section A: Accelerators, Spectrometers, Detectors and Associated Equipment*, 2011, **659**, 387 – 393.

26 B. Blau, K. N. Clausen, S. Gvasalaliya, M. Janoschek, S. Janssen, L. Keller, B. Roessli, J. Scheffer, P. Tregenna-Piggott, W. Wagner and O. Zaharo, *Neutron News*, 2009, **20**, 5.

27 M. Morgano, P. Trtik, M. Meyer, E. H. Lehmann, J. Hovind and M. Strobl, *Opt. Express*, 2018, **26**, 1809–1816.

28 C. Grünzweig, G. Frei, E. Lehmann, G. Kühne and C. David, *Rev. Sci. Instr.*, 2007, **78**, 053708.

29 S. C. Capelli and G. Romanelli, *J. Appl. Cryst.*, 2019, **52**, 1233–1237.

30 A. Borgschulte, F. Pendolino, R. Gremaud and A. Züttel, *Appl. Phys. Lett.*, 2009, **94**, 111907.

31 X. Wang, H. Zhang and W. Li, *Korean J. Chem. Eng.*, 2010, **27**, 1093 – 1098.

32 I. A. Fisher and A. T. Bell, *J. Catal.*, 1997, **172**, 222.

33 Y. Wang, S. Kattel, W. Gao, K. Li, P. Liu, J. G. Chen and H. Wang, *Nat. Comm.*, 2019, **10**, 1166.

34 P. C. H. Mitchell, S. F. Parker, A. J. Ramirez-Cuesta and J. Tomkinson, *Vibrational Spectroscopy with Neutrons With Applications in Chemistry, Biology, Materials Science and Catalysis.*, World Scientific Publishing, Singapore, 2005.

35 G. L. Griffin and J. T. Yates, *J. Chem. Phys.*, 1982, **77**, 3744.

36 J. Kiss, A. Witt, B. Meyer and D. Marx, *J. Phys. Chem.*, 2009, **130**, 184706.

37 K. H. Ernst, C. T. Campbell and G. Moretti, *J. Catal.*, 1992, **134**, 66.

38 L. C. Grabow and M. M. Mavrikakis, *ACS Catal.*, 2011, **1**, 365.

39 J. Biesdorf, P. Oberholzer, F. Bernauer, A. Kaestner, P. Vontobel, E. H. Lehmann, T. J. Schmidt and P. Boillat, *Phys. Rev. Lett.*, 2014, **112**, 248301.

40 T. Kandemir, M. Friedrich, S. F. Parker, F. Studt, D. Lennon, R. Schlögl and M. Behrens, *Phys. Chem. Chem. Phys.*, 2016, **18**, 17353.

41 I. P. Silverwood, N. G. Hamilton, C. J. Laycock, J. Z. Staniforth, R. M. Ormerod, C. D. Frost, S. F. Parker and D. Lennon, *Phys. Chem. Chem. Phys.*, 2010, **12**, 3102–3107.

42 I. P. Silverwood, N. G. Hamilton, A. McFarlane, R. M. Ormerod, T. Guidi, J. Bones, M. P. Dudman, C. M. Goodway, M. Kibble, S. F. Parker and D. Lennon, *Review of Scientific Instruments*, 2011, **82**, 034101.

43 Armaroli, T., Bécue, T. and Gautier, S., *Oil & Gas Science and Technology - Rev. IFP*, 2004, **59**, 215–237.

44 P. Kubelka and F. Munk, *Z. Tech. Phys.*, 1931, **12**, 593–601.

45 P. Kubelka, *J. Opt. Soc. Am.*, 1948, **38**, 448–457.

46 L. H. Little, *Infrared Spectra of Adsorbed Species*, Academic Press, NewYork, 1966, pp. 1933–1941.

47 J. J. Venter and M. A. Vannice, *Carbon*, 1988, **26**, 889–902.

48 C. Chen, W. Cheng and S. Lin, *Catal. Lett.*, 2000, **68**, 45–48.

49 W. Lin, K. M. Stocker and G. C. Schatz, *J. Am. Chem. Soc.*, 2017, **139**, 4663–4666.

50 J. Quan, F. Muttaqien, T. Kondo, T. Kozarashi, T. Mogi, T. Imabayashi, Y. Hamamoto, K. Inagaki, I. Hamada, Y. Morikawa and J. Nakamura, *Nat. Chem.*, 2019, **11**, 722–729.

51 K. Kobl, S. Thomas, Y. Zimmermann, K. Parkhomenko and A.-C. Roger, *Cat. Tod.*, 2016, **270**, 31–42.

52 T. S. Askgaard, J. N. Norskov, C. V. Ovesen and P. Stoltze, *J. Catal.*, 1995, **156**, 229.

53 A. V. Tarasov, F. Seitz, R. Schlögl and E. Frei, *ACS Catalysis*, 2019, **9**, 5537–5544.

54 J. Reichert, S. Maerten, K. Meltzer, A. Tremel, M. Baldauf, P. Wasserscheid and J. Albert, *Sustainable Energy Fuels*, 2019, **3**, 3399–3405.

55 J. Terreni, M. Trottmann, T. Franken, A. Heel and A. Borgschulte, *Energy Technol.*, 2019, **7**, 1801093.

56 E. W. Thiele, *Ind. Eng. Chem.*, 1939, **31**, 916–920.

57 J. C. Slaa, G. J. M. Weierink, J. G. van Ommen and J. R. H. Ross, *Cat. Today*, 1992, **12**, 481.

58 S. Kattel, P. J. Ramírez, J. G. Chen, J. A. Rodriguez and P. Liu, *Science*, 2017, **355**, 1296.

59 J. Nakamura, T. Fujitani, S. Kuld, S. Helveg, I. Chorkendorff and J. Sehested, *Science*, 2017, **357**, 6354.

60 K. Christmann, *Surf. Sci. Rep.*, 1988, **7**, 1.

61 K. W. Frese, *Surf. Sci.*, 1987, **182**, 85.

62 P. B. Rasmussen, P. M. Holmblad, H. Christoffersen, P. A. Taylor and I. Chorkendorff, *Surf. Sci.*, 1992, **287/288**, 79.

63 A. Borgschulte, R. Gremaud and R. Griessen, *Phys. Rev. B*, 2008, **78**, 094106.

64 N. Lopez, Z. Lodziana, F. Illas and M. Salmeron, *Phys. Rev. Lett.*, 2004, **93**, 146103.

65 C. G. Van de Walle, *Phys. Rev. Lett.*, 2000, **85**, 1012–1015.

66 C. G. Van de Walle and J. Neugebauer, *Nature*, 2003, **423**, 626–628.

67 G. Brauer, W. Anwand, D. Grambole, J. Grenzer, W. Skorupa, J. Cizek, J. Kuriplach, I. Prochazka, C. C. C. Ling, K. So, D. Schulz and D. Klimm, *Phys. Rev. B*, 2009, **79**, 115212.

68 M. G. Wardle, J. P. Goss and P. R. Briddon, *Phys. Rev. Lett.*, 2006, **96**, 205504.

69 H.-H. Nahm, C. H. Park and Y.-S. Kim, *Sci. Rep.*, 2014, **4**, 4124.

70 B. E. Hayden and C. L. A. Lamont, *Phys. Rev. Lett.*, 1989, **63**, 1823–1825.

71 J. Schumann, M. Eichelbaum, T. Lunkenbein, N. Thomas, M. C. Álvarez Galván, R. Schlögl and M. Behrens, *ACS Catalysis*, 2015, **5**, 3260–3270.

72 R. van den Berg, G. Prieto, G. Korpershoek, L. I. van der Wal, A. J. van Bunningen, S. Laegsgaard-Joergensen, P. E. de Jongh and K. P. de Jong, *Nat. Commun.*, 2016, **7**, 13057.

73 J. Nakamura, I. Nakamura, T. Uchijima, T. Watanabe and T. Fujitani, *Model studies of methanol synthesis on copper catalysts*, Elsevier, 1996, vol. 101, pp. 1389 – 1399.

74 F. Studt, M. Behrens, E. L. Kunkes, N. Thomas, S. Zander, A. Tarasov, J. Schumann, E. Frei, J. B. Varley, F. Abild-Pedersen, J. K. Nørskov and R. Schlögl, *ChemCatChem*, 2015, **7**, 1105–1111.

75 J. Terreni, O. Sambalova, S. Borgschulte, A.; Rudić, S. Parker and A. Ramirez-Cuesta, *Catalysts*, 2020, **10**, 433.

76 H. Magnusson and F. Frisk, *J. Phase Equilib. Diffus.*, 2017, **38**, 65–69.

Table 1 Hydrogen in and on Cu/ZnO. For visualization of the various sites see Fig. 9.

reaction	formula	heat of reaction	est. amount
surface adsorption	$\frac{1}{2}H_2 + Cu \rightarrow Cu \cdot H,$	$\Delta H_{(Cu)\cdot H} = -39$ kJ/mol[60]	$2 \cdot 10^{-2}$ mass %
bulk absorption	$\frac{1}{2x}H_2 + Cu \rightarrow CuH_x,$	$\Delta H_{CuH_x} = +48$ kJ/mol H[76]	$1 \cdot 10^{-7}$ mass %[76]
surface adsorption	$\frac{1}{2}H_2 + ZnO \rightarrow (ZnO) \cdot H,$	$\Delta H_{(ZnO)\cdot H} < 0$	$5 \cdot 10^{-2}$ mass %
bulk absorption	$\frac{1}{2x}H_2 + ZnO \rightarrow ZnOH_x,$	$\Delta H_{ZnOH_x} > 0$	$2 \cdot 10^{-1}$ mass %[67]
surface reduction	$\frac{3}{2}H_2 + ZnO \rightarrow Zn \cdot H + H_2O$	$\frac{2}{3}\left(-\Delta H_{ZnO} + \Delta H_{H_2O} + \Delta H_{Zn\cdot H}\right) > 0$	$x_H \simeq 0$, $\Delta m/M = -8.6$ mass%
bulk reduction	$H_2 + ZnO \rightarrow Zn + H_2O,$	$-\Delta H_{ZnO} + \Delta H_{H_2O} > 0$	$x_H \simeq 0$, $\Delta m/M = -20$ mass%